https://doi.org/10.5194/egusphere-2026-2445
Preprint. Discussion started: 13 May 2026

Continuous wintertime water vapor profiling by Raman lidar at Neumayer Station III, Antarctica: Characteristics of meridional moisture transport and assessment of ERA5 reanalysis

Friederike Jakob[1], Martin Radenz[1], Holger Baars[1], Patric Seifert[1], and Ronny Engelmann[1]
[1]Leibniz Institute for Tropospheric Research, Leipzig, Germany
Correspondence: Friederike Jakob (jakob@tropos.de)

Abstract. The vertical distribution of water vapor is essential for understanding moisture transport toward Antarctica, which influences the surface mass balance of the ice sheets via precipitation, sublimation and longwave radiation effects. However, high-resolution vertical water vapor observations remain limited. In this study, we present continuous water vapor mixing ratio (WVMR) profiles obtained with Raman lidar at Neumayer Station III, Antarctica during wintertime (May to August) 2023. The observations reveal a mean WVMR of $0.7\,\mathrm{g\,kg^{-1}}$ between 0 to 6 km and capture an exceptional moist air intrusion in early July with WVMR values reaching up to $3.9\,\mathrm{g\,kg^{-1}}$. Two dominant synoptic patterns driving moisture advection toward the Antarctic coast could be identified, producing distinctly different vertical moisture structures. Pattern A, with a low-pressure system northwest of Neumayer Station III seems to be more effective in transporting moisture than a low-pressure system northeast of the Station (pattern B). The lidar measurements are compared to ERA5 reanalysis humidity fields. While ERA5 generally reproduces the moisture distribution reasonably well, it exhibits a dry bias of $0.1\,\mathrm{g\,kg^{-1}}$ ($\approx 10\,\%$) in the lower troposphere. Potential causes of the bias were investigated. The bias shows no clear dependence on the air mass source region, but is dependent on the assimilation cycle, synoptic conditions and the surface type representation in ERA5. These findings suggest that limitations in the representation of boundary layer mixing processes are a major contributor to the observed dry bias. The results highlight the value of continuous high-resolution water vapor profiling in understanding Antarctic moisture transport and validating model-derived reanalysis products.

1 Introduction

Atmopsheric moisture distribution and transport toward the Antarctic continent are among the most crucial processes for understanding the atmospheric drivers of the mass balance of ice sheet and shelfs (Lenaerts et al., 2019). Direct impacts are either precipitation, direct deposition (both adding to the surface mass balance, SMB; Bromwich, 1988) or sublimation (negative term to the SMB; Déry and Yau, 2002). More complex interactions, such as the rate of sublimation of precipitation in dry sub-cloud layers (Grazioli et al., 2017; Gehring et al., 2022) or the magnitude of longwave downward radiation (e.g. Sato and Simmonds, 2021; Seidel et al., 2025) depend on the amount and vertical distribution of water vapor. Futhermore, the representation of water vapor has been linked to large intermodel differences in general circulation models in the southern-hemisphere extratropics (e.g., Po-Chedley et al., 2018). Moisture transport to the Antarctic continent is usually associated with

https://doi.org/10.5194/egusphere-2026-2445
Preprint. Discussion started: 13 May 2026

meridional flow, with the strongest events being atmospheric rivers (AR, Wille et al., 2025). Those AR events typically occur only a few days per year at any location in coastal Antarctica, but are subject to strong interannual variability. A maximum in AR landfall frequency is observed in Dronning Maud Land, East Antarctica, where enhanced moisture transport causes the strongest snow accumulation events (Gorodetskaya et al., 2014; Baiman et al., 2023; Radenz et al., 2024). The majority of currently available studies on moisture transport and AR rely on reanalysis products, i.e. the observations assimilated into a model framework (Naakka et al., 2021). However, detailed measurements of water vapor, especially the vertical distribution are scarce above the Southern Ocean and Antarctica. Radiosonde observations are still the most important source for profiles of water vapor content (Gorodetskaya et al., 2020). Due to the logistical effort required, radiosondes are routinely launched only once or twice per day at a few stations. Ground-based observations can provide the integrated water vapor by means of time delays in GNSS observations (e.g. Negusini et al., 2016) or microwave radiometers (e.g. Ricaud et al., 2015). Spaceborne sensors using sounders in the microwave (e.g. Johnsen et al., 2004; Zhang et al., 2025) or infrared region (e.g. Gettelman et al., 2006) or radio occultation (e.g. Shao et al., 2023) also provide vertically resolved water vapor observations, but are limited in their accuracy and (vertical) resolution (Fan et al., 2023).

However, the interaction between moist air masses from the lower latitudes and dry air from the continent's interior causes strong gradients in the water vapor mixing ratio (WMVR), even down to small scales. Thus, continuous vertically-resolved observations are needed to sufficiently characterize the water vapor fields over Antarctica. This study uses Raman lidar observations obtained at Neumayer Station III (70.67° S, 8.27° W, in the following referred to as Neumayer) in 2023 to understand the vertical structure of water vapor fields. The high temporal (30s) and vertical (7.5m) resolution allows for process studies on flow regimes and validation of reanalysis fields. In the following, the measurement method is briefly recapitulated, the field setup, calibration and data subsampling are described. The results section presents the continuous observations of water vapor profiles at Neumayer and describes two exemplary case studies on the observed moisture dynamics. Finally, a multi-month comparison to the ERA5 reanalysis is presented. In a concluding section, found biases and potential implications are discussed.

2 Raman lidar water vapor observations at Neumayer Station III

2.1 Campaign of OCEANET-Atmosphere

Ground-based remote-sensing observations of aerosol, clouds and precipitation were performed by OCEANET-Atmosphere at Neumayer Station III (70.67° S, 8.27° W; Wesche et al., 2016) in 2023 (Radenz et al., 2024) in the framework of the COALA (Continuous Observations of Aerosol-cLoud interaction in Antarctica) project to better understand the formation of clouds and precipitation at coastal Antarctica. OCEANET-Atmosphere is an ACTRIS (Aerosol, Clouds, and Trace Gases Research Infrastructure, Laj et al., 2024) mobile exploratory platform, which ensures quality-controlled and accessible data for the standard variables. Deployed were a comprehensive set of ground-based remote sensing instruments, namely a PollyXT multi-wavelength Raman polarization lidar, a HATPRO microwave radiometer (MWR), a Cimel sun and lunar photometer, a Mira-35 cloud radar, a scanning Doppler lidar LITRA-S, and an optical disdrometer Parsivel^2. Data was collected continuously throughout the whole year, including the Antarctic winter with a comprehensive description being provided in Radenz et al. (2024).

https://doi.org/10.5194/egusphere-2026-2445
Preprint. Discussion started: 13 May 2026

All these observations were done next to the longterm meteorological, radiation, and air chemistry in-situ observations at Neumayer, where also routine radiosonde launches are performed (König-Langlo and Loose, 2007). In the context of this study, the water vapor observations by PollyXT, HATPRO and the daily radiosonde launches are analyzed (which are not an ACTRIS-variable).

2.2 Raman lidar water vapor retrieval

The multiwavelength Raman and polarization lidar PollyXT (Engelmann et al., 2016) emits radiation at the three wavelengths 355 nm, 532 nm and 1064 nm and uses 12 channels to detect the backscattered light. The Raman lidar technique allows the detection of inelastic scattering by water vapor and nitrogen molecules at 407 nm and 387 nm, respectively, from which profiles of WVMR are retrieved (Whiteman, 2003; Wandinger, 2005). Raman water vapor measurements are limited to nighttime, because the high solar background dominates over the weak Raman signal. They are further constrained to cloud-free conditions or below cloud base, since the lidar cannot penetrate through clouds with an optical thickness greater than 3. The raw data has a temporal resolution of 30 s and vertical resolution of 7.5 m. No overlap correction is required, assuming identical overlap for both Raman channels (Foth et al., 2015). The WVMR $m_{\mathrm{H_2O}}$ is defined as ratio of water vapor to dry air:

$$m_{\mathrm{H_2O}} = \frac{\rho_{\mathrm{H_2O}}(z)}{\rho_{\mathrm{air}}(z)} \sim \frac{N_{\mathrm{H_2O}}(z)}{N_{\mathrm{N_2}}(z)} \tag{1}$$

$\rho_{\mathrm{H_2O}}$ and ρ_{air} are the mass densities of water vapor and dry air, $N_{\mathrm{H_2O}}$ and $N_{\mathrm{N_2}}$ their molecular number densities, and z is the height above the instrument. Since the Raman signal is proportional to the molecular number densities, the WVMR $m_{\mathrm{H_2O}}$ can be determined by the ratio of backscattered signals P of water vapor and nitrogen (Whiteman, 2003; Wandinger, 2005; Foth et al., 2015):

$$m_{\mathrm{H_2O}}(z) = C_{\mathrm{H_2O}} \cdot \frac{P_{\mathrm{H_2O}}(z)}{P_{\mathrm{N_2}}(z)} \cdot \frac{\exp[-\int_0^z \alpha_{\lambda_{\mathrm{N_2}}}(\xi)d(\xi)]}{\exp[-\int_0^z \alpha_{\lambda_{\mathrm{H_2O}}}(\xi)d(\xi)]} \tag{2}$$

$C_{\mathrm{H_2O}}$ is the calibration factor (determined in the following, Sect. 2.3), the second term the measured signal ratio, and the third accounts for the different atmospheric transmissions at $\lambda_{\mathrm{N_2}}$ and $\lambda_{\mathrm{H_2O}}$ with atmospheric extinction coefficients $\alpha_{\lambda_{\mathrm{N_2}}}$ and $\alpha_{\lambda_{\mathrm{H_2O}}}$. To enhance the signal-to-noise ratio (SNR), a temporal smoothing of 10 min and vertical smoothing of 5 bins (37.5m) is applied.

2.3 Calibration

The calibration factor $C_{\mathrm{H_2O}}$ converts the measured lidar signal ratio, corrected for the differential atmospheric transmission, into an actual WVMR. It is determined from collocated water vapor measurements obtained by radiosondes and MWR. During the campaign, VAISALA radiosondes (type RS41) were launched once per day at around 12:00 UTC. The RS41 GRUAN Data Product (RS41-GDP.1) was used for calibration (Schmithüsen, 2022; Sommer et al., 2022). Since lidar water vapor measurements are restricted to nighttime, radiosondes can only be used for calibration during periods of polar night or low solar background (Antarctic winter). Between 05 May and 01 September 2023, $C_{\mathrm{H_2O}}$ was obtained from linear fits between

https://doi.org/10.5194/egusphere-2026-2445
Preprint. Discussion started: 13 May 2026

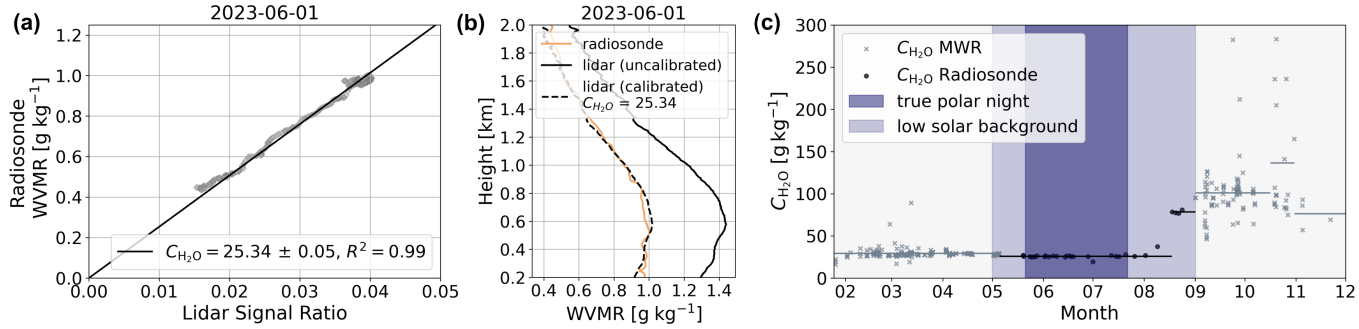

Figure 1. (a) WVMR measured by the radiosonde as a function of the lidar signal ratio, averaged over 20 min from 10:54 to 11:14 UTC on 1 June. The radiosonde was launched at 11:04 UTC. $C_{\mathrm{H_2O}}$ denotes the slope of the regression line, with the standard error of the slope, and R^2 is the coefficient of determination. (b) Height profile of the WVMR from the radiosonde (orange line) and the lidar, using the determined calibration constant (dashed line) and a default calibration constant (solid line). (c) All determined calibration constants over time, obtained from the radiosonde (black dots) and the MWR (grey crosses), with the six corresponding mean calibration constants as solid lines. The shaded area indicates the period of polar night (dark blue) or low solar background (light blue).

collocated radiosonde and lidar profiles. An example case from 1 June 2023 is shown in Fig. 1 demonstrating the linear regression (Fig. 1a) and the resulting calibrated lidar height profile (Fig. 1b). For each calibration case, lidar profiles were averaged over 20 minutes centered on the radiosonde launch time. Calibration cases were selected according to the following criteria: cloudfree conditions up to 2 km altitude and coefficient of determination of the linear regression $R^2 > 0.8$ for the height range 200–2000 m (reduced to 200–1000 m between 17 August and 01 September due to the lack of cloudfree cases around radiosonde launch time). In total, 29 cases met these criteria. Since the MWR provides continuous measurements of the integrated water vapor, it can also be used during periods without polar night when radiosondes could no longer be used for calibration (because launched at daytime conditions with too high solar background noise for the Raman lidar). Therefore, the MWR served as reference instrument for the remaining time period. An automatic calibration algorithm was applied, following Foth et al. (2015). The calibration constant can be affected by several factors, such as changes to the optical setup, the hardware or the instrument's housing. For example, a second window was temporarily installed for protection during snowstorms, which caused changes in the calibration constant. Consequently, six individual calibration constants were determined for the respective time periods (Fig. 1c). The radiosonde-derived calibration constants show very stable results during the polar night period, which is the period used for the subsequent analysis. Calculating the mean over all radiosonde-derived calibration constants for the respective time period yielded $C_{\mathrm{H_2O}} = 25.71 \pm 1.51$ g kg^{-1} ($\overline{R^2} = 0.92$) between 05 May and 17 August 2023 and $C_{\mathrm{H_2O}} = 78.42 \pm 1.48$ g kg^{-1} ($\overline{R^2} = 0.85$) between 17 August and 01 September. More details on the calibration of Raman lidar water vapor profiles are provided in Dai et al. (2018). The calibrated WVMR profiles are available via the PANGAEA database (https://doi.org/10.1594/PANGAEA.991540).

https://doi.org/10.5194/egusphere-2026-2445
Preprint. Discussion started: 13 May 2026

2.4 Subsampling to ERA5 grid

The Raman lidar WVMR measurements were compared to ERA5 (ECMWF fifth generation atmospheric reanalysis) data (Hersbach et al., 2020; Bell et al., 2021). To enable a consistent comparison between the high-resolution lidar observations and the coarser ERA5 fields, the lidar data was subsampled to the ERA5 grid. The ERA5 dataset (Hersbach et al., 2023a) provides a horizontal resolution of 0.25° × 0.25°, vertical spacing of 50 hPa on pressure levels, and in this study a temporal resolution of 2 h was used. Because the lidar reports height above ground level whereas ERA5 is defined on pressure levels, ERA5 profiles were converted to geometric height at each time step following the ERA5 documentation on computing geometric height from the geopotential heights. The lowest ERA5 level frequently yielded negative geometric heights due to low surface pressure and was therefore excluded. The second level, typically located between 100 to 200 m above ground, was used as the lowest comparison height. An upper bound of 6 km was chosen because WVMR retrievals above this altitude are often unreliable due to weak water vapor signal in the Raman channel. A cloud mask was applied to both datasets since the lidar provides WVMR data only under cloud-free conditions or below cloud base. Figure 2a presents the longterm time-height cross section of WVMR for the entire Antarctic winter. White regions mark periods and altitudes where no WVMR retrievals were available, either due to cloud presence or other data gaps, such as brief intervals at the beginning of May and end of August when daylight prevented measurements. The cloud mask was constructed in two steps. First, native-resolution lidar data was screened using SNR thresholds: profiles were discarded when the SNR fell below 2.5 at 407 nm or below 5 at 387 nm, conditions typically associated with clouds or insufficient Raman signal at high altitudes. The remaining lidar profiles were then averaged within each ERA5 grid cell to match the ERA5 spatial and temporal resolution. Second, a grid cell based validity check was applied. For each grid cell, the valid fraction of lidar data points ($N_{\mathrm{valid}}/N_{\mathrm{total}}$) was computed. Cells with a valid fraction below 0.9 were excluded, as these generally corresponded to cloud-contaminated regions. An exception was made for periods affected by automatic polarization calibration, which can also reduce the valid fraction, these cells were retained. Additionally, grid cells were removed when the standard deviation of the averaged WVMR exceeded $0.8\ \mathrm{g\,kg^{-1}}$, indicating potential cloud edges and thus unrealistically high WVMR values. All cloud mask parameters were chosen empirically to achieve robust results, allowing a proper comparison between the two datasets. The resulting mask is shown in Fig. 2b, indicated by the hatched areas. These periods were excluded from the analysis. Nevertheless, the remaining data provides sufficient coverage for an extensive comparison with ERA5, including adequate representation of cloudy and moist atmospheric conditions that were most affected by the masking procedure.

3 Results

3.1 High-resolution observations of moisture dynamics

Raman lidar water vapor measurements performed at Neumayer provide valuable insight into the moisture dynamics along the northern coast of Antarctica. The coastal atmosphere is primarily influenced by cold, dry air masses originating from the continental interior, but is also intermittently affected by warm, moist air intrusions from the Atlantic Ocean. During the

https://doi.org/10.5194/egusphere-2026-2445
Preprint. Discussion started: 13 May 2026

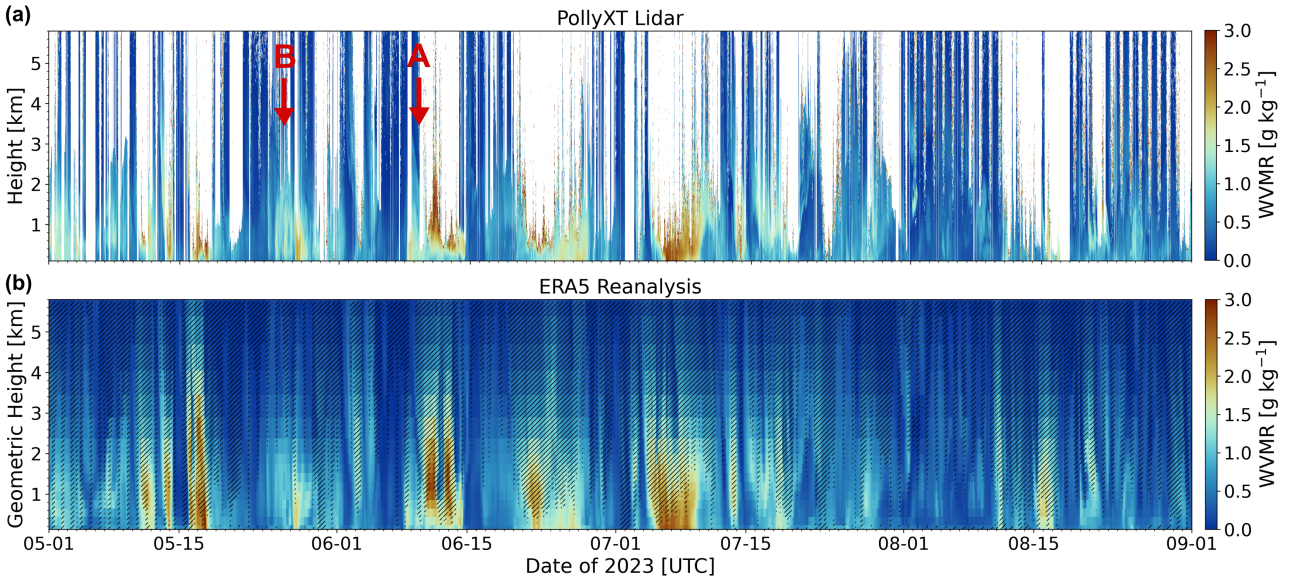

Figure 2. Time–height cross sections of WVMR for Antarctic winter. (a) Raman lidar WVMR retrievals, where white regions indicate periods and altitudes without valid measurements due to cloud attenuation, low signal-to-noise ratio, or daylight. (b) Corresponding ERA5 WVMR fields converted to geometric height, hatched areas mark the grid cells identified by the cloud mask.

analyzed period from May to August 2023 (Antarctic winter), WVMR values in the 0–6 km height range typically ranged between 0 and 3 $\mathrm{g\,kg^{-1}}$, with a mean value of 0.7 $\mathrm{g\,kg^{-1}}$ (Fig. 2a). For reference, a WVMR value of 0.7 $\mathrm{g\,kg^{-1}}$ corresponds to a relative humidity of approximately 32 % at −20 °C and 850 hPa. August was the driest month, with maximum values of 2.2 $\mathrm{g\,kg^{-1}}$ and a mean WVMR of 0.48 $\mathrm{g\,kg^{-1}}$. An extraordinary moist air intrusion occurred in early July, with WVMR values reaching up to 3.9 $\mathrm{g\,kg^{-1}}$, influenced by an AR event.

Two dominant synoptic patterns were identified as the primary drivers of warm, moist air advection toward the Antarctic coast in winter 2023 (Fig. 3a and b). Periods of moist air advection were defined based on vertically averaged WVMR values exceeding 1 $\mathrm{g\,kg^{-1}}$ within 0 to 2 km for at least 8 hours. According to this criterion, a total of 11 moist air events were identified, corresponding to approximately 28 days during the analyzed period. The associated synoptic patterns were classified manually based on the prevailing wind direction and the large-scale pressure distribution derived from ERA5 reanalysis data. In pattern A (Fig. 3a), a low-pressure system is located northwest of Neumayer producing direct onshore advection of warm and moist air masses from the South Atlantic. A representative lidar measurement of this weather regime is provided in Fig. 3c, illustrating the WVMR on 9 June between 0.1 km and 6 km altitude. The first half of the day exhibits a very dry free troposphere with increasing moisture in the boundary layer. During the second half of the day, continuous moist air advection leads to the formation of low-level clouds in the afternoon, as evidenced by the completely attenuated lidar signal. In case B (Fig. 3b), the low-pressure system is positioned northeast of Neumayer. This pattern is characterized by an indirect onshore transport of previously advected maritime air masses along the Antarctic coast. The corresponding example case (Fig. 3d) shows a

https://doi.org/10.5194/egusphere-2026-2445
Preprint. Discussion started: 13 May 2026

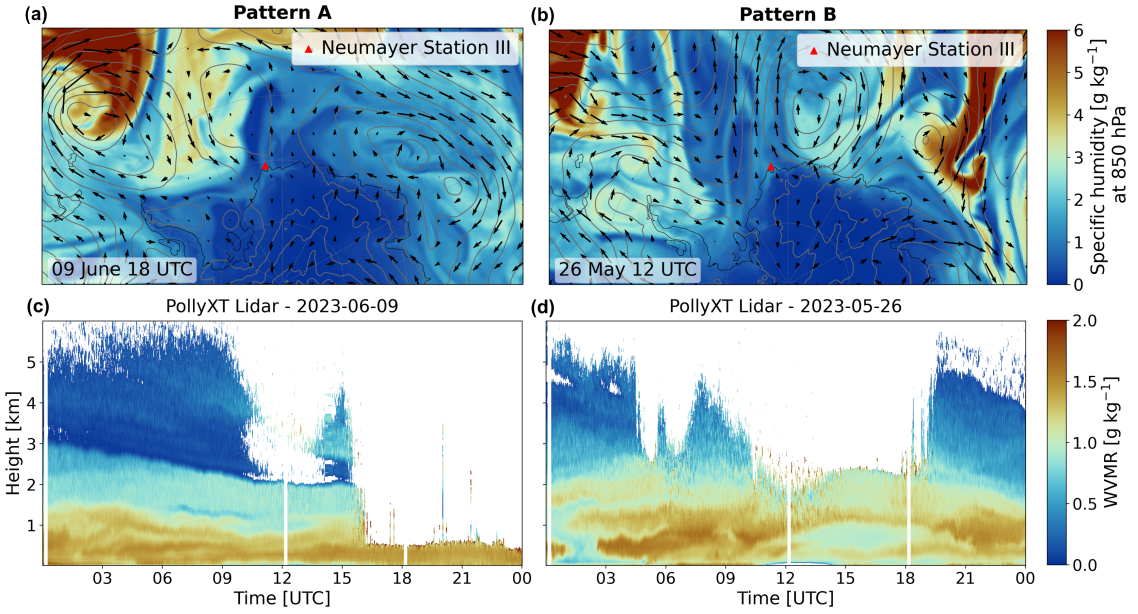

Figure 3. Upper panel: ERA5 reanalysis specific humidity (color shading), geopotential (grey lines) and wind vectors at 850 hPa for two synoptic patterns: (a) Pattern A on 9 June 2023 at 18 UTC and (b) Pattern B on 26 May 2023 at 12 UTC. Lower panel: Time-height cross section of WVMR measured by the PollyXT Raman lidar for representative example days corresponding to each pattern: (c) 9 June 2023 (Pattern A) and (d) 26 May 2023 (Pattern B).

fragmented and patchy moisture distribution, with two distinct moisture plumes occurring around 07 UTC and 22 UTC, and several drier periods in between. Cloud formation is observed around noon. The contrast between these two patterns is striking: while case A exhibits a deep and continuous moisture layer throughout the advection event, with the highest moisture close to the surface, case B produces a much more variable and discontinuous moisture structure, including moisture inversions. This difference likely results from the coastal transport pathway in case B, during which the maritime air mass undergoes continuous mixing with dry continental air, creating a highly variable moisture field. In contrast, case A represents more direct oceanic influence. During the analyzed period, approximately 17 % of the time the synoptic situation could be associated with pattern A, 30% with pattern B, and 53 % with other weather regimes, which were mainly characterized by advection of dry continental air from the southwest. However, considering only the identified moist air events, 42 % correspond to pattern A, 40 % to pattern B, and approximately 18 % to other patterns. Notably, the strong moist air intrusion in July was also associated with pattern A. This suggests that pattern A is more effective at transporting relatively moist air toward Antarctica's coast, although it occurs less frequently than pattern B.

https://doi.org/10.5194/egusphere-2026-2445
Preprint. Discussion started: 13 May 2026

3.2 Comparison with ERA5 reanalysis

Continuous high-resolution Raman lidar measurements of the WVMR provide an excellent opportunity to evaluate reanalysis data. Here, we compare our WVMR measurements with the ERA5 reanalysis humidity product. The preparation of both data sets for a consistent comparison is described in Sect. 2.4. Figure 4 shows the resulting time-height cross sections of the masked ERA5 data and the masked and subsampled lidar data (Panel a, b). The comparison was performed by calculating the difference in WVMR ($m_{\mathrm{H_2O,ERA5}} - m_{\mathrm{H_2O,Lidar}}$) for each grid cell, yielding the absolute differences. The result is shown in Fig. 4c. Overall, the two data sets agree reasonably well. However, Fig. 4c reveals substantial local discrepancies, reaching up to $\pm 1\,\mathrm{g\,kg^{-1}}$. Although the differences are predominantly negative, indicating that ERA5 tends to underestimate humidity, sporadic larger positive deviations also occur. The pronounced moist air intrusion in July appears as a distinct feature that is poorly represented in ERA5. Further discrepancies are evident in the vertical moisture structure and variability. The Raman lidar data exhibits sharper gradients (e.g., 2–4 June) and higher variability, especially within very dry layers (e.g., 15–16 June), despite being averaged and downsampled to match the ERA5 resolution. Moreover, moist layers, particularly near the surface, are sometimes completely absent in the ERA5 reanalysis (e.g., 23–27 June), and differences in vertical structure are also apparent (e.g., 14 June). A time–height cross section for June, highlighting the aforementioned days, is provided in the Appendix (Fig. A1).

To quantify these differences systematically, a statistical analysis was conducted. The mean absolute and relative (magnitude of absolute difference divided by the measured WVMR) differences were computed as a function of height for the entire analysis period (1 May–30 September) within the 0.1 to 6 km altitude range. Figure 5a presents the vertical profiles of both absolute and relative differences between ERA5 and lidar WVMR measurements. The absolute differences reveal a distinct vertical structure: they are largest within the boundary layer, reaching approximately $-0.1\,\mathrm{g\,kg^{-1}}$ near the surface, indicating that ERA5 underestimates humidity most strongly in the lower troposphere. Between 2 and 4 km, the absolute differences decrease and approach zero, suggesting better agreement in the mid-troposphere. Above 4 km, the absolute differences increase again, though this is primarily attributable to very low WVMR values at these heights where even small absolute deviations translate to larger relative errors. The relative difference profile shows considerable variability with altitude but generally varies around 10% throughout the troposphere, with larger relative deviations occurring near the surface and at higher altitudes where moisture content is extremely low. Overall, ERA5 exhibits a systematic dry bias of approximately $0.1\,\mathrm{g\,kg^{-1}}$ in the lower troposphere. A linear regression analysis shows good agreement between the two datasets, when taking all heights and the whole period into account (Fig. 5b). With a fixed slope of 1, the linear regression yields an offset of $-0.08\,\mathrm{g\,kg^{-1}}$, confirming the systematic dry bias in ERA5. The scatter plot reveals that while there is generally good correlation between the datasets, a considerable spread is evident, particularly at WVMR values above $1.0\,\mathrm{g\,kg^{-1}}$. The majority of points fall below the 1:1 line, visually confirming ERA5's tendency to underestimate WVMRs.

To investigate potential causes of this dry bias, we first examined its dependence on the air mass source. For this analysis, the TRACE latitude bands product (see Appendix B) was used (reception height of 2 km) to derive height profiles of the mean WVMR and the absolute difference in WVMR grouped by their dominant air mass source. For each time step, the

https://doi.org/10.5194/egusphere-2026-2445
Preprint. Discussion started: 13 May 2026

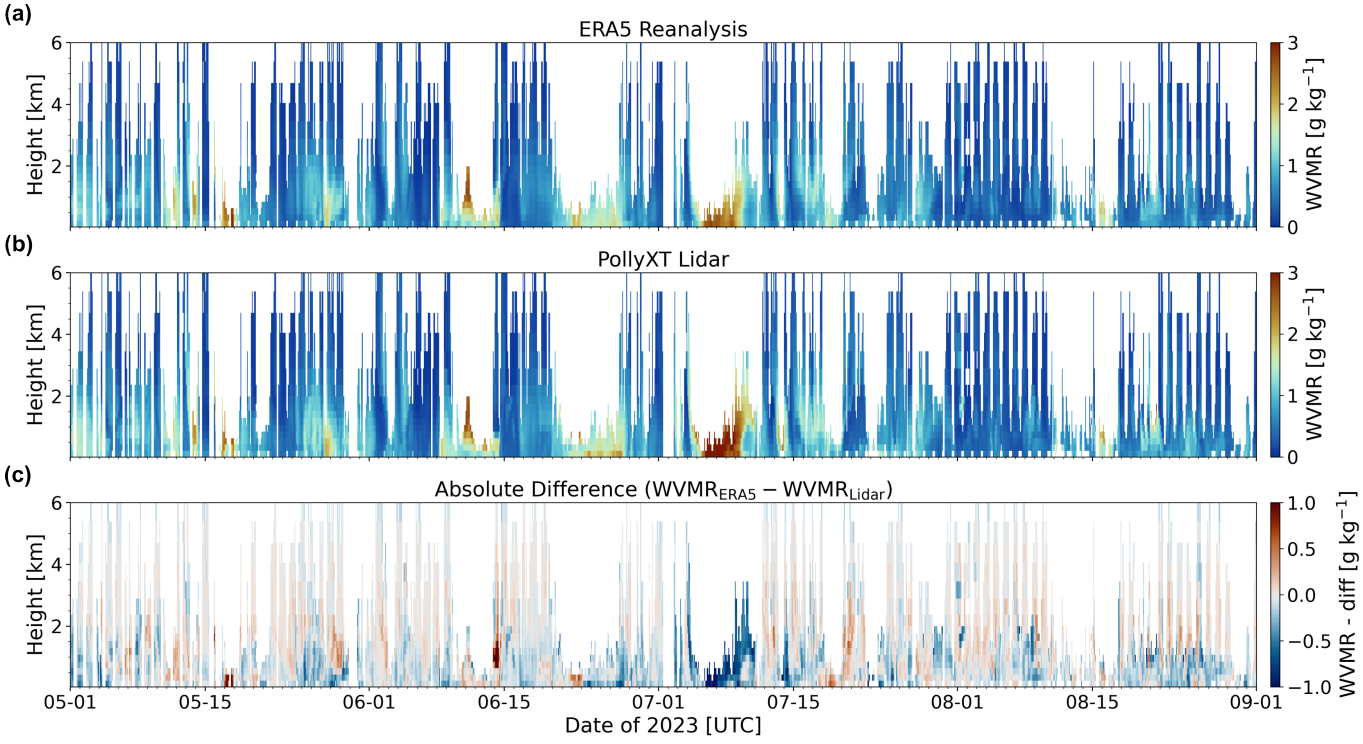

Figure 4. Time-height cross sections of WVMR sampled to ERA5 grid for the measurement period May to August 2023 with a cloud mask applied to all datasets. Panel (a) shows ERA5 reanalysis, (b) PollyXT lidar measurements subsampled to ERA5 grid, and (c) the absolute difference in WVMR between ERA5 reanalysis and PollyXT lidar measurements.

dominant source region was defined by the maximum residence time, and the corresponding WVMR profile was assigned to that region. Mean height profiles and their standard deviations were then calculated for each air mass source category. Figure 6a shows the mean lidar WVMR profiles. Air masses originating from lower latitudes generally contain more moisture than those from higher latitudes. While high-latitude air masses exhibit a relatively narrow distribution, air masses from the mid-latitudes show broader variability, indicating that they advect both very moist as well as relatively dry air masses. Figure 6b presents the absolute difference in WVMR between ERA5 and PollyXT measurements. No systematic difference in the bias is observed between the mid-latitude and high-latitude air mass categories. Although the mid-latitudes again show a broader spread, allowing for larger negative and positive deviations, overall the bias does not seem to depend on the air mass source region. Similar results were obtained when using other TRACE products, like the land surface classification or geographical areas.

A second potential factor is the dependence of the bias on the ERA5 data assimilation cycle. The relative and absolute differences between the Raman lidar and ERA5 water vapor profiles were calculated separately for the day (09–21 UTC) and night (21–09 UTC) assimilation cycles (Figs. 7a and b). When considering only the day assimilation cycle, both the

https://doi.org/10.5194/egusphere-2026-2445
Preprint. Discussion started: 13 May 2026

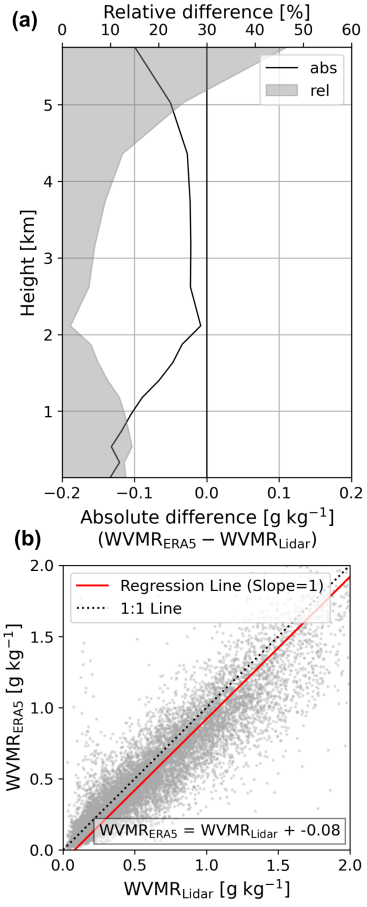

Figure 5. (a) Height profile showing the mean absolute difference (black line) and relative difference (grey shading; magnitude of absolute difference divided by measured WVMR) in WVMR between ERA5 reanalysis and PollyXT lidar measurements, averaged over the measurement period May to August 2023. Panel (b) shows scatterplot of WVMR comparing ERA5 reanalysis with PollyXT lidar measurements over the same period between 0.1 to 6 km. The black dotted line indicates the 1:1 line, and the red line shows a regression fit with fixed slope of 1.

relative and absolute differences increased compared to the results obtained using all data, with the largest deviations occurring between 1 and 2 km altitude. In contrast, the corresponding differences during the night assimilation cycle were slightly smaller. More observational data, such as radiosonde and satellite measurements, are available for assimilation during the day, whereas the night cycle primarily relies on satellite data alone, because radiosondes at Neumayer are nominally launched only at 12 UTC. Therefore, one would expect the reanalysis to show better agreement with independent observations during the day. However, our analysis reveals the opposite pattern, with a larger bias during the day assimilation cycle when more observations are available. Beyond the assimilation cycle, synoptic-scale conditions may also influence the ERA5 reanalysis performance. To assess this effect, we investigated the impact of the strong moist air intrusion event that occurred in early July 2023 by excluding the period affected by this event (4–10 July 2023) from the dataset. The resulting comparison is shown in

https://doi.org/10.5194/egusphere-2026-2445
Preprint. Discussion started: 13 May 2026

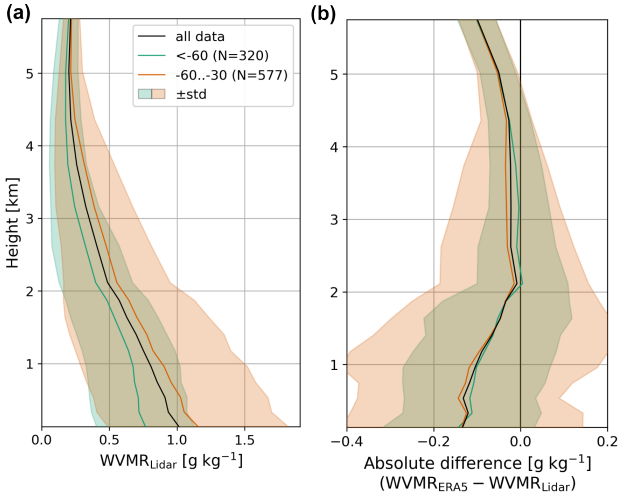

Figure 6. Height profiles and standard deviation of mean (a) WVMR and (b) absolute difference in WVMR between ERA5 and PollyXT lidar measurements calculated for the dominant airmass source (maximum residence time) derived from TRACE latitude product (color) and for all profiles (black).

Fig. 7c. After removing this episode, a clear improvement in the agreement between the Raman lidar and ERA5 profiles was observed, particularly in the lower troposphere. A t-test was applied to assess the statistical significance of these differences ($p_{\mathrm{day}} = 2.4 \cdot 10^{-4}$, $p_{\mathrm{night}} = 0.50$, $p_{\mathrm{moist,air}} = 4.0 \cdot 10^{-8}$). Among these factors, the exclusion of the moist air intrusion had by far the most significant effect, highlighting the strong influence of such remarkable synoptic events on the reanalysis bias.

Another potential factor contributing to the observed bias is the representation of the surface in ERA5. Neumayer is situated on a floating ice shelf, with the open ocean approximately $20\,\mathrm{km}$ to the north and the Antarctic inland to the south. The ERA5 reanalysis provides the variable "land-sea mask" (Hersbach et al., 2023b), which defines the ratio of land to ocean or inland waters (e.g., lakes, reservoirs, rivers, and coastal waters) within each model grid cell. This dimensionless parameter ranges from 0 (entirely ocean) to 1 (entirely land), with intermediate values indicating a mixture of land and water. The land-sea mask determines whether a grid cell is treated as land or ocean/inland waters in the model physics and data assimilation. The grid cell containing Neumayer has a land-sea mask value of 0.75, meaning that ERA5 treats it predominantly as land but with an ocean component. To investigate the influence of this classification, the Raman lidar observations at Neumayer were compared with ERA5 reanalysis data from two additional grid points: one 0.42° north of the station, defined as completely ocean (land-sea mask = 0), and another 0.33° to the south, defined as completely land (land-sea mask = 1). For these two grid points, the same procedure as described in Sect. 2.4 was applied. The differences between the Raman lidar observations and ERA5 reanalysis for the ocean and land grid points were calculated as a function of height and time, then averaged over the analyzed period to produce height profiles of the mean absolute and relative differences (Figs. 8a and b). For the land grid point, the differences between ERA5 and the lidar observations are substantially larger than for the Neumayer grid cell, indicating a stronger dry

https://doi.org/10.5194/egusphere-2026-2445
Preprint. Discussion started: 13 May 2026

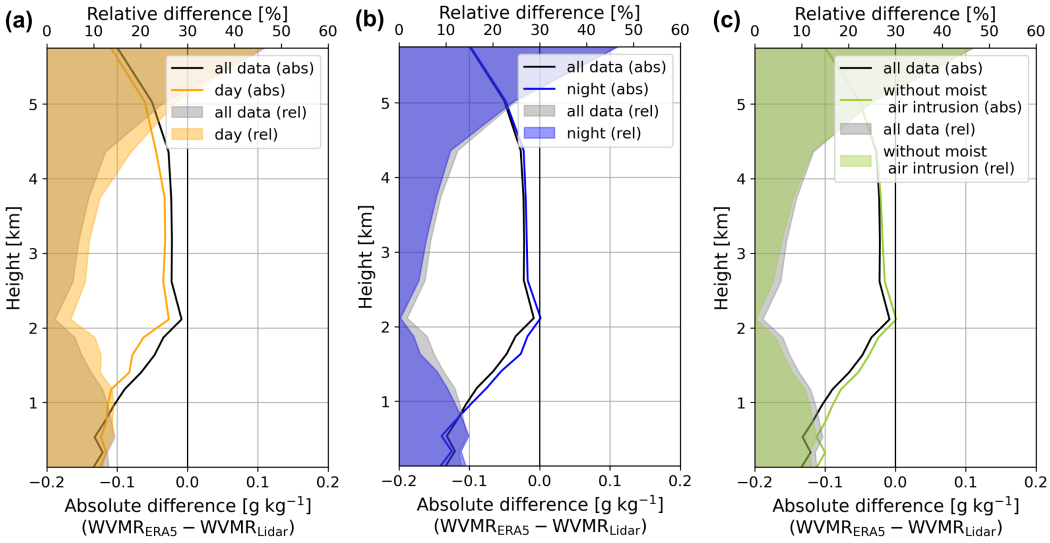

Figure 7. Height profiles of mean absolute (solid lines) and relative (shaded areas; magnitude of absolute difference divided by measured WVMR) differences in WVMR between ERA5 reanalysis and PollyXT lidar measurements. Panels show measurements for (a) daytime assimilation cycle (09 to 21 UTC), (b) nighttime assimilation cycle (21 to 09 UTC), and (c) the dataset excluding the moist air intrusion period from 04 to 10 July 2023. Black lines and gray shading represent all data (May to Aug 2023), while orange, blue, and green lines and shading indicate the respective subsets.

bias that extends throughout the lower troposphere. In contrast, the ocean grid point shows markedly smaller deviations, with both the absolute and relative difference remaining close to zero throughout the entire height range.

4 Summary & Conclusions

This study presents the first continuous high-resolution water vapor profiling observations at Neumayer obtained by Raman lidar. The multi-month observations during Antarctic winter (May to August) 2023 capture the vertical structure and temporal variability of moisture at Antarctica's coast during wintertime. The atmosphere above Neumayer is characterized by very dry background conditions (mean WVMR of $0.7\,\mathrm{g\,kg^{-1}}$), interrupted by episodes of moisture intrusions, including an exceptional moist air intrusion in early July 2023. Two characteristic synoptic regimes were identified as primary drivers governing moisture transport toward Antarctica's coast. Pattern A is associated with a low-pressure system northwest of Neumayer and produces deep and continuous moisture layers, which can be linked to the direct advection of warm, moist air masses from the South Atlantic to Neumayer. Pattern B, featuring a low-pressure system northeast of Neumayer, leads to indirect onshore transport of previously advected maritime air masses. This dynamic situation produces more fragmented and variable vertical moisture structures due to the interaction of moist oceanic air masses with dry continental outflow. Although Pattern B appears to be more frequent, Pattern A seems to be more effective in producing atmospheric river conditions, as it was associated with the

https://doi.org/10.5194/egusphere-2026-2445
Preprint. Discussion started: 13 May 2026

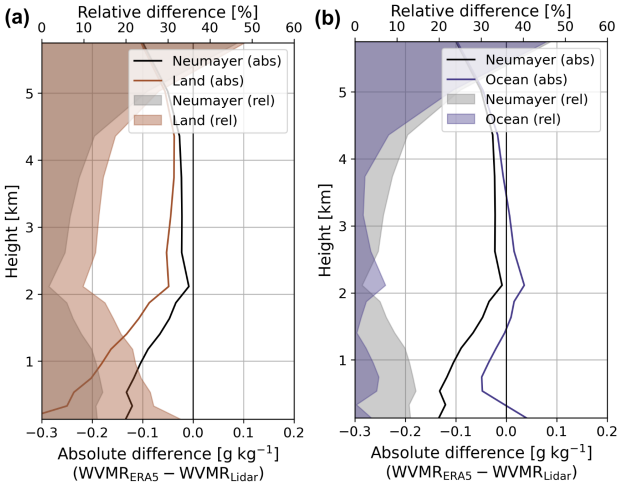

Figure 8. Height profiles of the mean absolute (solid lines) and relative (shaded areas; magnitude of absolute difference divided by measured WVMR) differences in WVMR between ERA5 and PollyXT lidar measurements for different ERA5 surface-type representations. (a) Comparison using the ERA5 grid cell classified as land and (b) comparison using the grid cell classified as ocean, each contrasted with the Neumayer grid cell.

strongest moist air intrusion event during the measurement period. However, Clem et al. (2020) observed an increased cyclonal activity in the Weddell Sea between 1997 and 2018, therefore direct moisture advection events (pattern A) might become more frequent, potentially increasing the occurrence of strong moist-air intrusions in the future. The detailed comparison with the ERA5 reanalysis data shows generally good agreement with lidar measurements, although the observations reveal sharper vertical gradients and greater variability than the reanalysis, even after spatial and temporal averaging to the ERA5 grid. A systematic dry bias of $0.1\ \mathrm{g\,kg^{-1}}$ in the lower troposphere (up to 2 km) was identified, confirmed by a linear regression offset of $-0.08\ \mathrm{g\,kg^{-1}}$ across all heights. This bias exhibits several notable dependencies. The systematic deviation is larger during the daytime assimilation cycle than during nighttime, a surprising result given the greater observational data availability for daytime assimilation. The bias is also substantially impacted by extreme moist air intrusion events, with statistical analysis confirming that such synoptic conditions exert the strongest influence on reanalysis performance. The systematic error also seems to show a clear dependence on surface type representation of the reanalysis. Reanalysis grid cells classified as pure ocean (north of Neumayer) show better agreement with lidar measurements than the grid cell containing Neumayer, while grid cells classified as pure land (south of Neumayer) exhibit an even larger dry bias. This suggests that the surface classification (and thus model physics) in ERA5 contributes to the dry bias and points to possible limitations in the representation of boundary layer mixing processes in ERA5, of course assuming that the Raman lidar observations are also representative for the neighboring grid cells. The bias shows no dependence on the air mass source, indicating that large-scale moisture transport is well represented in ERA5. This supports the hypothesis that the observed bias is probably more related to local boundary layer parameterizations.

https://doi.org/10.5194/egusphere-2026-2445
Preprint. Discussion started: 13 May 2026

Overall, the results presented in this study underscore the value of high-resolution water vapor observations in understanding atmospheric moisture dynamics in Antarctica and evaluating reanalysis products. The calibrated Raman lidar WVMR profiles obtained during the COALA campaign at Neumayer are now publicly available, enabling further analysis and research. Highly resolved longterm water vapor observations at Antarctica will become increasingly important for understanding the vertical distribution of water vapor and its role in precipitation, deposition, sublimation, and longwave radiative processes that govern impacts on Antarctica's ice sheet and shelfs.

Data availability. The complete dataset (16 January to 31 December 2023) of calibrated Raman lidar WVMR profiles at Neumayer Station III, Antarctica is available at the PANGAEA database (https://doi.org/10.1594/PANGAEA.991540). The radiosonde data used was obtained from the GRUAN data base (Sommer et al., 2022, RS41-GDP.1). The ERA5 reanalysis data used in this study is available for download from the Climate Data Store (Hersbach et al., 2023a).

https://doi.org/10.5194/egusphere-2026-2445
Preprint. Discussion started: 13 May 2026

Appendix A: Details on the observed structural differences between ERA5 and lidar

To provide more details on the structural differences observed between ERA5 reanalysis and lidar measurements, a detailed comparison for June 2023 is presented below (Fig. A1). This case study provides additional insight into the characteristics discussed in Sect. 3.2.

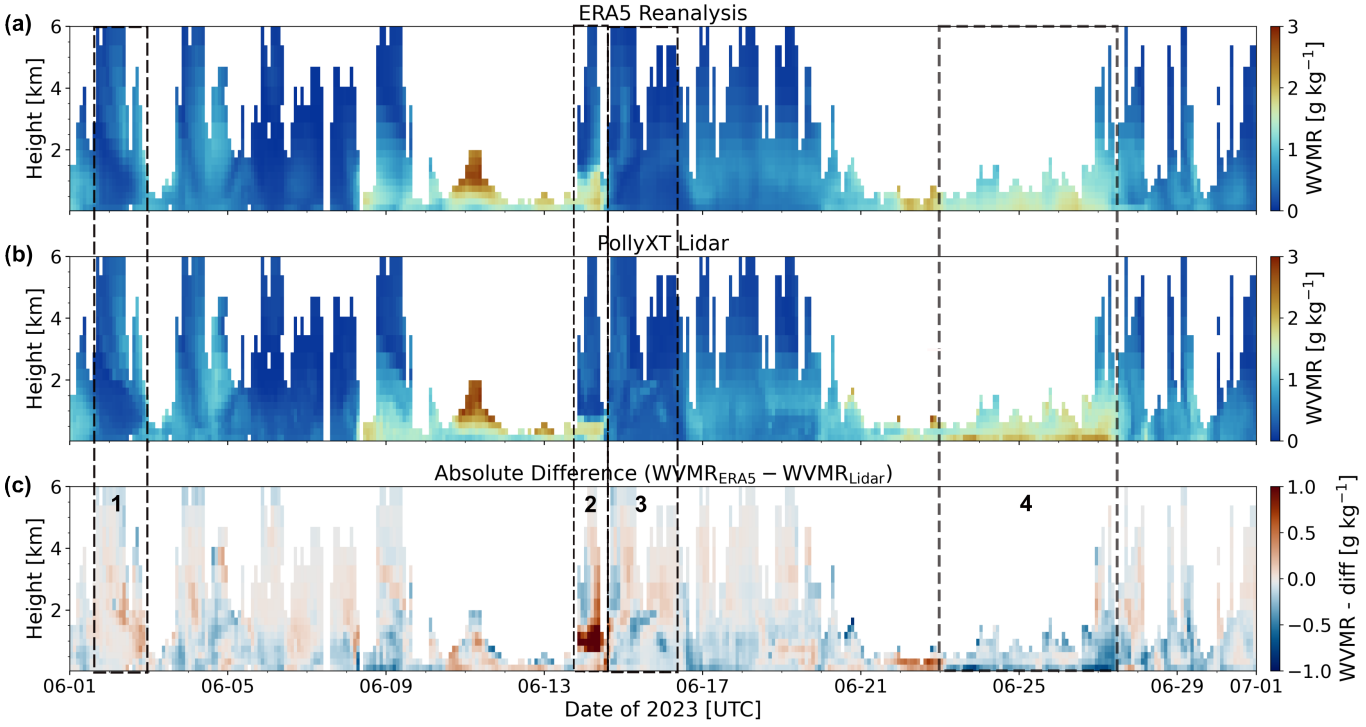

Figure A1. Time-height cross sections of WVMR sampled to ERA5 grid for June 2023 with a cloud mask applied to all datasets. Panel (a) shows ERA5 reanalysis, (b) PollyXT lidar measurements subsampled to ERA5 grid, and (c) the absolute difference in WVMR between ERA5 reanalysis and PollyXT lidar measurements. Dash rectangles mark the structural differences between ERA5 reanalysis and lidar measurements mentioned in Sect. 3.2 for 1: 2–4 June, 2: 14 June, 3: 15–16 June and 4: 23–27 June.

https://doi.org/10.5194/egusphere-2026-2445
Preprint. Discussion started: 13 May 2026

Appendix B: Air mass source estimate

The automated time-height-resolved air mass source attribution described by Radenz et al. (2021a, b) is used to characterize air mass origin for the OCEANET-Atmosphere observations. As in the original publication, 10 d FLEXPART backward simulations with 500 particles are done in intervals of 3 h and 500 m throughout the period of the campaign. For the calculation of the residence times, a reception height of 2 km is used. Meridional transport is characterized by the 'latitude bands' product, which groups the air mass source into latitudes south of 60°S and 60-30°S (Fig. B1).

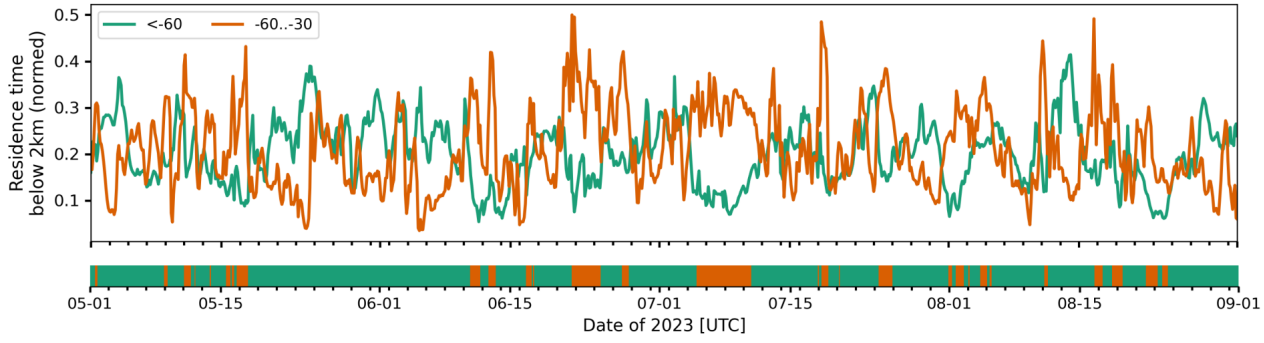

Figure B1. Time series of the mean residence time for the 'latitude bands' product between 0 and 6 km height for a reception height of 2 km height. Shown is the same time period as Fig. 2 and 4. The color bar below indicates the time periods that are used to assign the dominant air mass source for the analysis in Fig. 6

https://doi.org/10.5194/egusphere-2026-2445
Preprint. Discussion started: 13 May 2026

Author contributions. FJ performed the data analysis and drafted the manuscript under supervision of MR, HB and PS. MR and RE conducted the measurements at Neumayer Station III. All authors were involved in the discussion of results and the writing process.

Competing interests. The authors declare that they have no conflict of interest.

Acknowledgements. We would like to acknowledge the ERA5 reanalysis provided by the European Centre for Medium-Range Weather Forecasting. We thank the Alfred Wegener Institute as well as the technical and logistical personnel of Neumayer Station III, especially the wintering team 2023 for their support (AWI_NM_2023, AWI_ANT_22). Especially Lukas Muser, who was responsible for the meteorological observations, in particular the radiosonde launches. We are grateful to Holger Schmithüsen for supervising the meteorological observatory and providing guidance on data usage. MR's work was partly funded by the priority program 1158 "Antarctic Research with Comparative Investigations in Arctic Ice Areas" of Deutsche Forschungsgemeinschaft (Funding 463307613). OCEANET-Atmosphere is part of ACTRIS-D, which is funded by the Federal Ministry of Education and Research of Germany (BMBF) under the FONA Strategy "Research for Sustainability" (funding code 01LK2001A). BMBF also funded hardware components under the funding code 01LK1603A.

https://doi.org/10.5194/egusphere-2026-2445
Preprint. Discussion started: 13 May 2026

References

Baiman, R., Winters, A. C., Lenaerts, J., and Shields, C. A.: Synoptic Drivers of Atmospheric River Induced Precipitation Near Dronning Maud Land, Antarctica, Journal of Geophysical Research: Atmospheres, 128, https://doi.org/10.1029/2022jd037859, 2023.

Bell, B., Hersbach, H., Simmons, A., Berrisford, P., Dahlgren, P., Horányi, A., Muñoz-Sabater, J., Nicolas, J., Radu, R., Schepers, D., Soci, C., Villaume, S., Bidlot, J., Haimberger, L., Woollen, J., Buontempo, C., and Thépaut, J.: The ERA5 global reanalysis: Preliminary extension to 1950, Quarterly Journal of the Royal Meteorological Society, 147, 4186–4227, https://doi.org/10.1002/qj.4174, 2021.

Bromwich, D. H.: Snowfall in high southern latitudes, Reviews of Geophysics, 26, 149–168, https://doi.org/10.1029/rg026i001p00149, 1988.

Clem, K. R., Fogt, R. L., Turner, J., Lintner, B. R., Marshall, G. J., Miller, J. R., and Renwick, J. A.: Record warming at the South Pole during the past three decades, Nature Climate Change, 10, 762–770, https://doi.org/10.1038/s41558-020-0815-z, 2020.

Dai, G., Althausen, D., Hofer, J., Engelmann, R., Seifert, P., Bühl, J., Mamouri, R.-E., Wu, S., and Ansmann, A.: Calibration of Raman lidar water vapor profiles by means of AERONET photometer observations and GDAS meteorological data, Atmospheric Measurement Techniques, 11, 2735–2748, https://doi.org/10.5194/amt-11-2735-2018, 2018.

Déry, S. J. and Yau, M. K.: Large-scale mass balance effects of blowing snow and surface sublimation, Journal of Geophysical Research: Atmospheres, 107, https://doi.org/10.1029/2001jd001251, 2002.

Engelmann, R., Kanitz, T., Baars, H., Heese, B., Althausen, D., Skupin, A., Wandinger, U., Komppula, M., Stachlewska, I. S., Amiridis, V., Marinou, E., Mattis, I., Linné, H., and Ansmann, A.: The automated multiwavelength Raman polarization and water-vapor lidar PollyXT: the neXT generation, Atmospheric Measurement Techniques, 9, 1767–1784, https://doi.org/10.5194/amt-9-1767-2016, 2016.

Fan, R., Zeng, Z., Wang, X., Zhang, L., Cheng, W., and Ding, M.: Comprehensive Evaluation and Comparison of AIRS, VASS, and VIRR Water Vapor Products Over Antarctica, Journal of Geophysical Research: Atmospheres, 128, https://doi.org/10.1029/2023jd039221, 2023.

Foth, A., Baars, H., Di Girolamo, P., and Pospichal, B.: Water vapour profiles from Raman lidar automatically calibrated by microwave radiometer data during HOPE, Atmospheric Chemistry and Physics, 15, 7753–7763, https://doi.org/10.5194/acp-15-7753-2015, 2015.

Gehring, J., Vignon, , Billault-Roux, A., Ferrone, A., Protat, A., Alexander, S. P., and Berne, A.: Orographic Flow Influence on Precipitation During an Atmospheric River Event at Davis, Antarctica, Journal of Geophysical Research: Atmospheres, 127, https://doi.org/10.1029/2021jd035210, 2022.

Gettelman, A., Walden, V. P., Miloshevich, L. M., Roth, W. L., and Halter, B.: Relative humidity over Antarctica from radiosondes, satellites, and a general circulation model, Journal of Geophysical Research: Atmospheres, 111, https://doi.org/10.1029/2005jd006636, 2006.

Gorodetskaya, I. V., Tsukernik, M., Claes, K., Ralph, M. F., Neff, W. D., and Van Lipzig, N. P. M.: The role of atmospheric rivers in anomalous snow accumulation in East Antarctica, Geophysical Research Letters, 41, 6199–6206, https://doi.org/10.1002/2014gl060881, 2014.

Gorodetskaya, I. V., Silva, T., Schmithüsen, H., and Hirasawa, N.: Atmospheric River Signatures in Radiosonde Profiles and Reanalyses at the Dronning Maud Land Coast, East Antarctica, Advances in Atmospheric Sciences, 37, 455–476, https://doi.org/10.1007/s00376-020-9221-8, 2020.

Grazioli, J., Madeleine, J.-B., Gallée, H., Forbes, R. M., Genthon, C., Krinner, G., and Berne, A.: Katabatic winds diminish precipitation contribution to the Antarctic ice mass balance, Proceedings of the National Academy of Sciences, 114, 10 858–10 863, https://doi.org/10.1073/pnas.1707633114, 2017.

Hersbach, H., Bell, B., Berrisford, P., Hirahara, S., Horányi, A., Muñoz-Sabater, J., Nicolas, J., Peubey, C., Radu, R., Schepers, D., Simmons, A., Soci, C., Abdalla, S., Abellan, X., Balsamo, G., Bechtold, P., Biavati, G., Bidlot, J., Bonavita, M., De Chiara, G., Dahlgren, P., Dee,

https://doi.org/10.5194/egusphere-2026-2445
Preprint. Discussion started: 13 May 2026

D., Diamantakis, M., Dragani, R., Flemming, J., Forbes, R., Fuentes, M., Geer, A., Haimberger, L., Healy, S., Hogan, R. J., Hólm, E., Janisková, M., Keeley, S., Laloyaux, P., Lopez, P., Lupu, C., Radnoti, G., de Rosnay, P., Rozum, I., Vamborg, F., Villaume, S., and Thépaut, J.: The ERA5 global reanalysis, Quarterly Journal of the Royal Meteorological Society, 146, 1999–2049, https://doi.org/10.1002/qj.3803, 2020.

Hersbach, H., Bell, B., Berrisford, P., Biavati, G., Horányi, A., Muñoz Sabater, J., Nicolas, J., Peubey, C., Radu, R., Rozum, I., Schepers, D., Simmons, A., Soci, C., Dee, D., and Thépaut, J.-N.: ERA5 hourly data on pressure levels from 1940 to present, https://doi.org/10.24381/cds.bd0915c6, Copernicus Climate Change Service (C3S) Climate Data Store (CDS) [data set] (Accessed on 28-Mar-2025), 2023a.

Hersbach, H., Bell, B., Berrisford, P., Biavati, G., Horányi, A., Muñoz Sabater, J., Nicolas, J., Peubey, C., Radu, R., Rozum, I., Schepers, D., Simmons, A., Soci, C., Dee, D., and Thépaut, J.-N.: ERA5 hourly data on single levels from 1940 to present, https://doi.org/10.24381/cds.adbb2d47, Copernicus Climate Change Service (C3S) Climate Data Store (CDS) [data set] (Accessed on 30-Jun-2025), 2023b.

Johnsen, K.-P., Miao, J., and Kidder, S.: Comparison of atmospheric water vapor over Antarctica derived from CHAMP/GPS and AMSU-B data, Physics and Chemistry of the Earth, Parts A/B/C, 29, 251–255, https://doi.org/10.1016/j.pce.2004.01.005, 2004.

König-Langlo, G. and Loose, B.: The Meteorological Observatory at Neumayer Stations $GvNandNM-II$ Antarctica, Polarforschung, 76, 25–38, https://doi.org/10.2312/polarforschung.76.1-2.25, 2007.

Laj, P., Lund Myhre, C., Riffault, V., Amiridis, V., Fuchs, H., Eleftheriadis, K., Petäjä, T., Salameh, T., Kivekäs, N., Juurola, E., Saponaro, G., Philippin, S., Cornacchia, C., Alados Arboledas, L., Baars, H., Claude, A., De Mazière, M., Dils, B., Dufresne, M., Evangeliou, N., Favez, O., Fiebig, M., Haeffelin, M., Herrmann, H., Höhler, K., Illmann, N., Kreuter, A., Ludewig, E., Marinou, E., Möhler, O., Mona, L., Eder Murberg, L., Nicolae, D., Novelli, A., O'Connor, E., Ohneiser, K., Petracca Altieri, R. M., Picquet-Varrault, B., van Pinxteren, D., Pospichal, B., Putaud, J.-P., Reimann, S., Siomos, N., Stachlewska, I., Tillmann, R., Voudouri, K. A., Wandinger, U., Wiedensohler, A., Apituley, A., Comerón, A., Gysel-Beer, M., Mihalopoulos, N., Nikolova, N., Pietruczuk, A., Sauvage, S., Sciare, J., Skov, H., Svendby, T., Swietlicki, E., Tonev, D., Vaughan, G., Zdimal, V., Baltensperger, U., Doussin, J.-F., Kulmala, M., Pappalardo, G., Sorvari Sundet, S., and Vana, M.: Aerosol, Clouds and Trace Gases Research Infrastructure (ACTRIS): The European Research Infrastructure Supporting Atmospheric Science, Bulletin of the American Meteorological Society, 105, E1098–E1136, https://doi.org/10.1175/bams-d-23-0064.1, 2024.

Lenaerts, J. T. M., Medley, B., van den Broeke, M. R., and Wouters, B.: Observing and Modeling Ice Sheet Surface Mass Balance, Reviews of Geophysics, 57, 376–420, https://doi.org/10.1029/2018rg000622, 2019.

Naakka, T., Nygård, T., and Vihma, T.: Air Moisture Climatology and Related Physical Processes in the Antarctic on the Basis of ERA5 Reanalysis, Journal of Climate, 34, 4463–4480, https://doi.org/10.1175/jcli-d-20-0798.1, 2021.

Negusini, M., Petkov, B. H., Sarti, P., and Tomasi, C.: Ground-Based Water Vapor Retrieval in Antarctica: An Assessment, IEEE Transactions on Geoscience and Remote Sensing, 54, 2935–2948, https://doi.org/10.1109/tgrs.2015.2509059, 2016.

Po-Chedley, S., Armour, K. C., Bitz, C. M., Zelinka, M. D., Santer, B. D., and Fu, Q.: Sources of Intermodel Spread in the Lapse Rate and Water Vapor Feedbacks, Journal of Climate, 31, 3187–3206, https://doi.org/10.1175/jcli-d-17-0674.1, 2018.

Radenz, M., Seifert, P., Baars, H., Floutsi, A. A., Yin, Z., and Bühl, J.: Automated time–height-resolved air mass source attribution for profiling remote sensing applications, Atmospheric Chemistry and Physics, 21, 3015–3033, https://doi.org/10.5194/acp-21-3015-2021, 2021a.

https://doi.org/10.5194/egusphere-2026-2445
Preprint. Discussion started: 13 May 2026

Radenz, M., Bühl, J., Seifert, P., Baars, H., Engelmann, R., Barja González, B., Mamouri, R.-E., Zamorano, F., and Ansmann, A.: Hemispheric contrasts in ice formation in stratiform mixed-phase clouds: disentangling the role of aerosol and dynamics with ground-based remote sensing, Atmospheric Chemistry and Physics, 21, 17 969–17 994, https://doi.org/10.5194/acp-21-17969-2021, 2021b.

Radenz, M., Engelmann, R., Henning, S., Schmithüsen, H., Baars, H., Frey, M. M., Weller, R., Bühl, J., Jimenez, C., Roschke, J., Muser, L. O., Wullenweber, N., Zeppenfeld, S., Griesche, H., Wandinger, U., and Seifert, P.: Ground-Based Remote Sensing of Aerosol, Clouds, Dynamics, and Precipitation in Antarctica: First Results from the 1-Year COALA Campaign at Neumayer Station III in 2023, Bulletin of the American Meteorological Society, 105, E1438–E1457, https://doi.org/10.1175/bams-d-22-0285.1, 2024.

Ricaud, P., Grigioni, P., Zbinden, R., Attié, J.-L., Genoni, L., Galeandro, A., Moggio, L., Montaguti, S., Petenko, I., and Legovini, P.: Review of tropospheric temperature, absolute humidity and integrated water vapour from the HAMSTRAD radiometer installed at Dome C, Antarctica, 2009–14, Antarctic Science, 27, 598–616, https://doi.org/10.1017/s0954102015000334, 2015.

Sato, K. and Simmonds, I.: Antarctic skin temperature warming related to enhanced downward longwave radiation associated with increased atmospheric advection of moisture and temperature, Environmental Research Letters, 16, 064 059, https://doi.org/10.1088/1748-9326/ac0211, 2021.

Schmithüsen, H.: Radiosonde measurements from Neumayer Station (1983-02 et seq), https://doi.org/10.1594/PANGAEA.940584, PANGAEA [data set], 2022.

Seidel, C., Althausen, D., Ansmann, A., Wendisch, M., Griesche, H., Radenz, M., Hofer, J., Dahlke, S., Maturilli, M., Walbröl, A., Baars, H., and Engelmann, R.: Close Correlation Between Vertically Integrated Tropospheric Water Vapor and the Downward, Broadband Thermal-Infrared Irradiance at the Ground: Observations in the Central Arctic During MOSAiC, Journal of Geophysical Research: Atmospheres, 130, https://doi.org/10.1029/2024jd042378, 2025.

Shao, X., Ho, S.-P., Jing, X., Zhou, X., Chen, Y., Liu, T.-C., Zhang, B., and Dong, J.: Characterizing the tropospheric water vapor spatial variation and trend using 2007–2018 COSMIC radio occultation and ECMWF reanalysis data, Atmospheric Chemistry and Physics, 23, 14 187–14 218, https://doi.org/10.5194/acp-23-14187-2023, 2023.

Sommer, M., von Rohden, C., Simeonov, T., Dirksen, R., Fiedler-Krüger, M., Friedrich, H., Körner, S., Naebert, T., Oelsner, P., and Tietz, R.: RS41 GRUAN Data Product Version 1 (RS41-GDP.1), https://doi.org/10.5676/GRUAN/RS41-GDP.1, 2022.

Wandinger, U.: Raman lidar, in: Lidar: range-resolved optical remote sensing of the atmosphere, pp. 241–271, Springer, 2005.

Wesche, C., Weller, R., König-Langlo, G., Fromm, T., Eckstaller, A., Nixdorf, U., and Kohlberg, E.: Neumayer III and Kohnen Station in Antarctica operated by the Alfred Wegener Institute, Journal of large-scale research facilities JLSRF, 2, A85, https://doi.org/10.17815/jlsrf-2-152, 2016.

Whiteman, D. N.: Examination of the traditional Raman lidar technique. II. Evaluating the ratios for water vapor and aerosols, Applied optics, 42, 2593–2608, 2003.

Wille, J. D., Favier, V., Gorodetskaya, I. V., Agosta, C., Baiman, R., Barrett, J. E., Barthelemy, L., Boza, B., Bozkurt, D., Casado, M., Chyhareva, A., Clem, K. R., Codron, F., Datta, R. T., Durán-Alarcón, C., Francis, D., Hoffman, A. O., Kolbe, M., Krakovska, S., Linscott, G., Maclennan, M. L., Mattingly, K. S., Mu, Y., Pohl, B., Santos, C. L.-D., Shields, C. A., Toker, E., Winters, A. C., Yin, Z., Zou, X., Zhang, C., and Zhang, Z.: Atmospheric rivers in Antarctica, Nature Reviews Earth amp; Environment, 6, 178–192, https://doi.org/10.1038/s43017-024-00638-7, 2025.

Zhang, Z., Brown, S., and Colliander, A.: Retrieval of atmospheric water vapor and temperature profiles over Antarctica from satellite microwave observations using an iterative approach, The Cryosphere, 19, 4011–4026, https://doi.org/10.5194/tc-19-4011-2025, 2025.